

## Chapter 6

# Wavelet-Based Multiscale Enveloping

The use of enveloping technique has been found in many engineering fields. For example, enveloping is employed for the detection of ultrasonic signals, as seen in nondestructive testing (McGonnagle 1966; Greguss 1980; Liang et al 2006). It also presents a complementary tool to spectral analysis in detecting structural defects in rolling bearings (e.g., surface spalling) and gearbox (e.g., broken teeth) (Tse et al 2001; Wang 2001). Generally, three steps are involved in envelope extraction, as illustrated in Fig. 6.1. First, the measured signal passes through a band-pass filter with its bandwidth covering the high-frequency components of interest. As a result, the rest of the frequency components outside of the passing band are rejected, leaving only bursts of the band-passed components in the signal, as shown in Fig. 6.1b. Next, the band-passed signal is rectified, and shown in Fig. 6.1c. Finally, the rectified signal passes through a low-pass filter that is designed to allow only the low-frequency envelope of the signal to pass through, as shown in Fig. 6.1d.

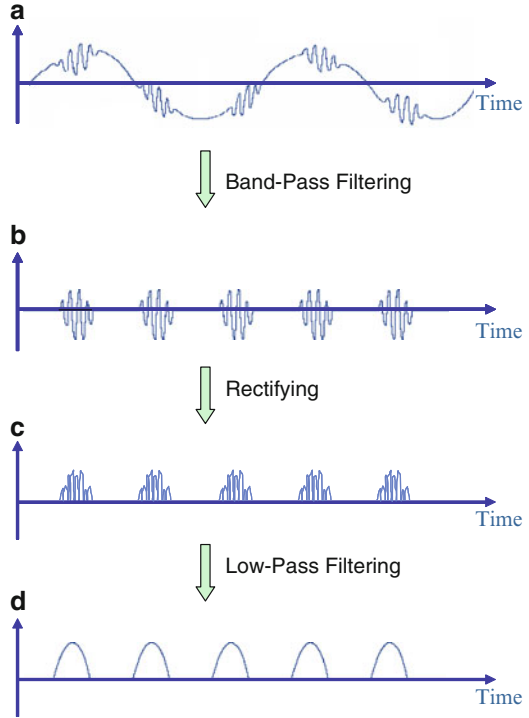
A limitation when applying this technique is that it requires a proper filtering band to be chosen to accurately extract the signal's envelope, for which a priori knowledge of the signal is desired. In this chapter, an adaptive, multiscale enveloping technique based on the wavelet transform is introduced, which overcomes the limitation of the conventional enveloping technique.

### 6.1 Signal Enveloping Through Hilbert Transform

The Hilbert transform has shown to present a good alternative to the conventional enveloping technique in extracting a signal's envelope (Hahn 1996). Mathematically, the Hilbert transform of a real-valued signal is defined as

$$\tilde{x}(t) = H[x(t)] = \int_{-\infty}^{\infty} \frac{x(\tau)}{\pi(t - \tau)} d\tau \quad (6.1)$$

**Fig. 6.1** Procedure for traditional envelope extraction



where  $H[\cdot]$  denotes the Hilbert transform operator. The symbol  $\tilde{x}(t)$  represents the Hilbert transform result of a real-valued signal  $x(t)$ , and is the convolution of  $x(t)$  and  $(1/\pi t)$ :

$$\tilde{x}(t) = x(t) \otimes \frac{1}{\pi t} \quad (6.2)$$

where the symbol  $\otimes$  denotes the “convolution” operation. According to the convolution theorem, the Fourier transform of the convolution of two signals is the product of the respective Fourier transforms of the two signals (Oppenheim et al. 1999). Accordingly, the Fourier transform of  $\tilde{x}(t)$  can be expressed as

$$\tilde{X}(f) = X(f) \times F\left[\frac{1}{\pi t}\right] \quad (6.3)$$

where the symbol  $\times$  denotes the “product” operation,  $X(f)$  is the Fourier transform of the signal  $x(t)$ , and  $F[1/\pi t]$  denotes the Fourier transform of the term  $1/\pi t$ . Specifically, this is defined as

$$F\left[\frac{1}{\pi t}\right] = -j \operatorname{sgn} f = \begin{cases} -j & f > 0 \\ 0 & f = 0 \\ j & f < 0 \end{cases} \quad (6.4)$$

Combining (6.4) with (6.3) yields

$$\tilde{X}(f) = \begin{cases} -jX(f) & f > 0 \\ 0 & f = 0 \\ jX(f) & f < 0 \end{cases} \quad (6.5)$$

Through an inverse Fourier transform performed on (6.5), the Hilbert transform of the real-valued signal can be realized. Accordingly, a special type of complex-valued signal  $z(t)$  can now be formulated as

$$z(t) = x(t) + j\tilde{x}(t) \quad (6.6)$$

with the real-valued signal  $x(t)$  being its real part, and the Hilbert transform of the signal,  $\tilde{x}(t)$ , being the imaginary part. Because of the inherent linearity property of the Fourier transform, the corresponding expression of (6.6) in the frequency domain can then be given as

$$Z(f) = X(f) + j\tilde{X}(f) \quad (6.7)$$

Combining (6.7) with (6.5) yields

$$Z(f) = X(f) + j \begin{cases} -jX(f) & f > 0 \\ 0 & f = 0 \\ jX(f) & f < 0 \end{cases} = \begin{cases} 2X(f) & f > 0 \\ X(0) & f = 0 \\ 0 & f < 0 \end{cases}. \quad (6.8)$$

Equations (6.6) and (6.8) indicate that the complex-valued signal  $z(t)$  is analytic in nature (Lawrence 1999). This means that it can also be expressed in terms of the complex polar coordinates as

$$z(t) = a(t) e^{j\theta(t)} \quad (6.9)$$

where

$$a(t) = \sqrt{x(t)^2 + \tilde{x}(t)^2} \quad (6.10)$$

$$\theta(t) = \tan^{-1} \left( \frac{\tilde{x}(t)}{x(t)} \right) \quad (6.11)$$

Equations (6.10) and (6.11) are called amplitude envelope function and instantaneous phase function of the signal  $x(t)$ , respectively. This indicates that performing the Hilbert transform on a real-valued signal  $x(t)$ , results in the formulation of a corresponding analytic signal  $z(t)$ , from which the envelope  $a(t)$  of the signal can be extracted. Such a property of the Hilbert transform makes it well suited for enveloping, as described in the following section.

## 6.2 Multiscale Enveloping Using Complex-Valued Wavelet

Among various base wavelets commonly used for signal analysis (Lee and Tang 1999; Yen and Lin 2000; Yoshida et al. 2000; Prabhakar et al. 2002; Yan and Gao 2005a), the complex-valued wavelets have the property of being analytic in nature. Such wavelets are generally defined as

$$\psi(t) = \psi_R(t) + j\psi_I(t) = \psi_R(t) + jH[\psi_R(t)] \quad (6.12)$$

where  $\psi_R(t)$  and  $\psi_I(t)$  represent the real and the imaginary parts of the complex-valued wavelet, respectively, and  $\psi_I(t)$  is the Hilbert transform of  $\psi_R(t)$ .

The wavelet transform  $wt_c(s, \tau)$  of a signal  $x(t)$  using complex-valued wavelet is expressed as

$$wt_c(s, \tau) = wt_R(s, \tau) + jwt_I(s, \tau) = wt_R(s, \tau) + jH[wt_R(s, \tau)] \quad (6.13)$$

where  $wt_R(s, \tau)$  and  $wt_I(s, \tau)$  are the real and imaginary parts of the transformation results, respectively. They are defined as

$$\begin{cases} wt_R(s, \tau) = |s|^{-1/2} \int_{-\infty}^{\infty} x(t) \psi_R^*\left(\frac{t-\tau}{s}\right) dt \\ wt_I(s, \tau) = H[wt_R(s, \tau)] = |s|^{-1/2} \int_{-\infty}^{\infty} x(t) H\left[\psi_R^*\left(\frac{t-\tau}{s}\right)\right] dt \end{cases} \quad (6.14)$$

Equations (6.13) and (6.14) indicate that the results of wavelet transform  $wt_c(s, \tau)$  of a signal  $x(t)$  using the complex-valued wavelet is also analytic. As a result, the signal's envelope at scale  $s$ ,  $env_{wt}(s, \tau)$ , can be readily calculated from the modulus of the wavelet coefficients as

$$env_{wt}(s, \tau) = \|wt_c(s, \tau)\| = \sqrt{wt_R(s, \tau)^2 + H[wt_R(s, \tau)]^2} \quad (6.15)$$

As the wavelet transform itself can be considered as a series of band-pass filtering operations (implemented through the scaled parameter  $s$ ) as described in Chap. 3, and the signal's envelope can be obtained by calculating the modulus of the wavelet coefficients when the complex-valued wavelet is used, a multiscale

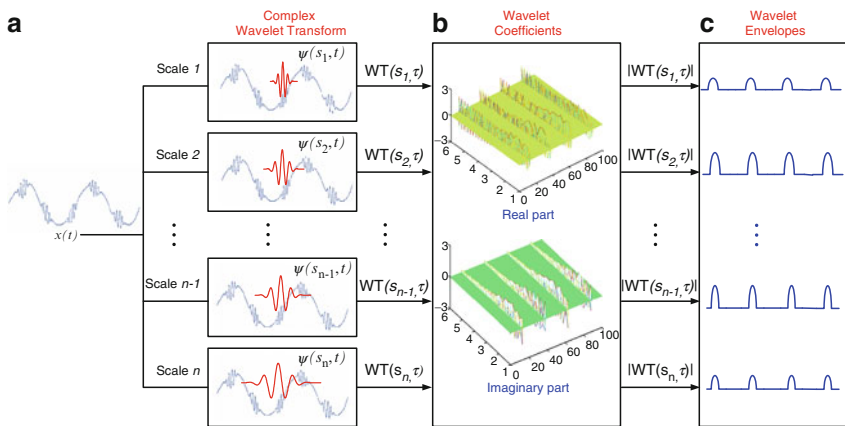


**Fig. 6.2** Illustration of the multiscale enveloping algorithm

enveloping technique can be developed on the basis of the wavelet transform. Computationally, this technique first decomposes the signal (e.g., vibrations measured on a defective rolling bearing) into different wavelet scales by means of a complex-valued wavelet transform, as illustrated in Fig. 6.2a. A series of wavelet coefficients, which are expressed as real part and imaginary part, respectively, are then obtained (Fig. 6.2b). The envelope signal in each scale (Fig. 6.2c) is finally calculated from the modulus of the wavelet coefficients.

### 6.3 Application of Multiscale Enveloping

This section describes the application of the multiscale enveloping technique introduced above to two different mechanical systems.

#### 6.3.1 Ultrasonic Pulse Differentiation for Pressure Measurement in Injection Molding

Online monitoring and control of pressure in the cavity of an injection machine has been shown to be critically important for improving product quality while maintaining low rejection rates in injection molding (Rawabdeh and Petersen 1999). The design of a self-powered wireless sensor has enabled the placement of multiple sensors within a mold to achieve comprehensive spatial coverage of the cavity pressure profile (Gao et al. 2001; Theurer et al. 2001). To overcome electromagnetic shielding caused by the steel mold that surrounds the sensors, ultrasonic wave has been explored as an alternative to electromagnetic wave for pressure data

transmission out of the mold (Zhang et al. 2004). Specifically, mold cavity pressure measured by a piezoceramic sensing element is digitized into a series of ultrasonic pulse trains, with each pulse train representing the crossing of a preset pressure threshold. The actual cavity pressure (denoted as ❶ in Fig. 6.3a) is reconstructed by multiplying the total number of the pulse trains (denoted as ❸ in Fig. 6.3a) with the known threshold value. Given a matrix arrangement of such wireless sensors within the mold cavity, spatial coverage of the cavity pressure profile can be obtained. An example of a sensor matrix consisting of six wireless sensors and a single receiver is illustrated in Fig. 6.3b.

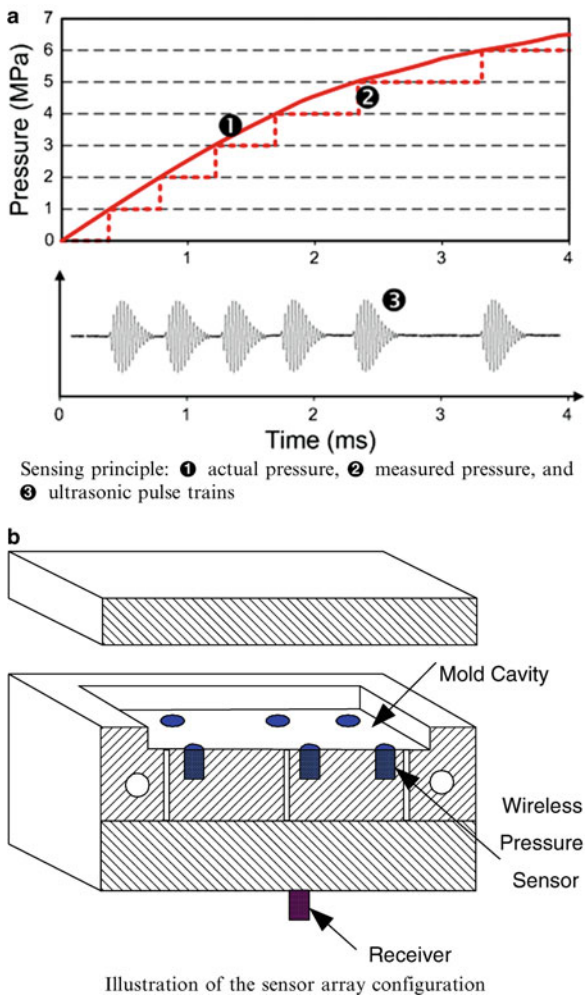


**Fig. 6.3** Sensing principle and the sensor array arrangement in an injection mold. (a) Sensing principle: ❶ actual pressure, ❷ measured pressure, and ❸ ultrasonic pulse trains and (b) illustration of the sensor array configuration

The limitation of such a 1D enveloping technique is illustrated in Fig. 6.4, which illustrates a total of six ultrasonic pulse trains generated by six transmitters, with the center frequencies being 2,210, 2,480, 2,785, 3,140, 3,530, and 3,980 kHz, respectively. Each pulse train is related to the crossing of the melt pressure of a threshold level at a specific location along the cavity. The envelope of the signal is given in Fig. 6.4b. By thresholding the enveloped signal, the time of arrival of each pulse train can be determined. However, as the difference in frequency of the pulse trains cannot be accurately resolved, the spectrum of the multiple pulse trains appears in Fig. 6.4c as a lumped group, giving the appearance as if they were generated by a single transmitter.

Such a problem can be solved by using the multiscale enveloping technique introduced in this chapter, which decomposes the pulse trains into individual frequency subbands and extracts the respective envelope from the pulse trains in each subband. Multiplying the number of crossings by the envelope with each

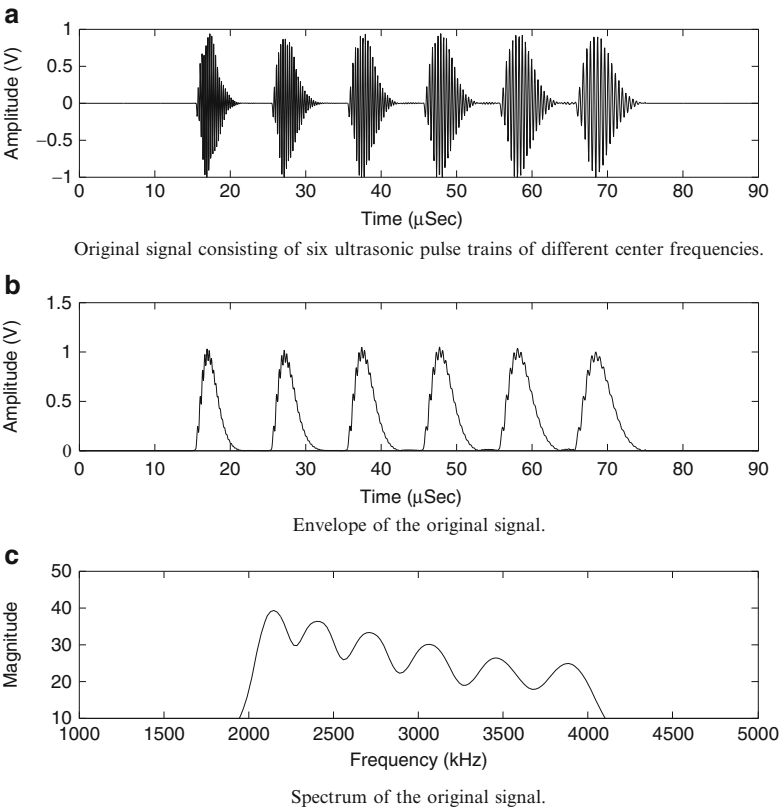


**Fig. 6.4** Limitation of 1D enveloping technique. (a) Original signal consisting of six ultrasonic pulse trains of different center frequencies, (b) envelope of the original signal, and (c) spectrum of the original signal

respective threshold value, the cavity pressure profile can be reconstructed. This is illustrated in the following sections, through both simulation and experiments.

### 6.3.1.1 Simulation

The performance of the multiscale enveloping for pulse detection on a sensor matrix consisting of six spatially distributed ultrasonic transmitters is evaluated first by means of a computer simulation. The six spectrally adjacent ultrasonic pulse trains are centered at 2,210, 2,480, 2,785, 3,140, 3,530, and 3,980 kHz, respectively, labeled as ① through ⑥ in Fig. 6.5. The pulses are separated by an interval of 10  $\mu\text{s}$  from one another, simulating the flow of polymer melt over the sensor matrix sequentially at a constant speed. As shown in Fig. 6.5, the six pulses could be detected and well separated into six levels (each level corresponds to a specific scale calculated on the basis of ultrasonic pulse center frequency) through a wavelet-based multiscale enveloping process.

In another simulation, the multiscale enveloping technique is applied to decomposing an ultrasonic signal consisting of two different types of ultrasound pulse trains:

1. spectrally identical (with the same center frequency of 3,980 kHz) and timely adjacent (5  $\mu\text{s}$  apart), as labeled ① and ② in Fig. 6.6a
2. timely overlapped and spectrally adjacent (with center frequencies of 2,210 and 2,785 kHz, respectively) as labeled ③ and ④ in Fig. 6.6a.

As shown in Fig. 6.6b, pulses ① and ② are successfully differentiated both spectrally (at the same level 6, because of their identical center frequency) and

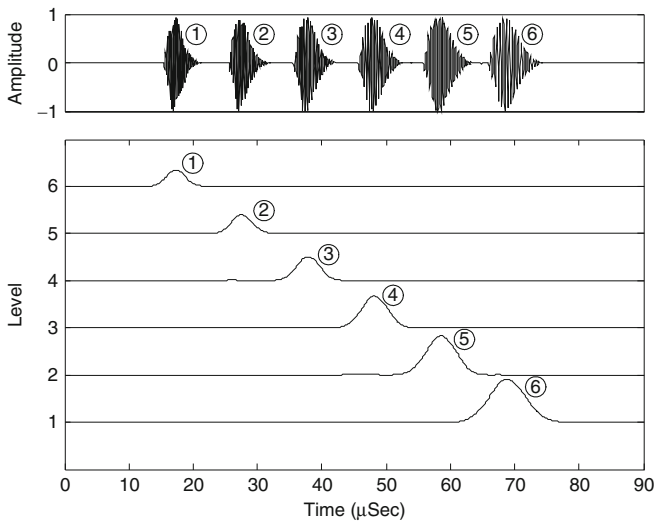


**Fig. 6.5** Detection and differentiation of six spectrally adjacent pulse trains



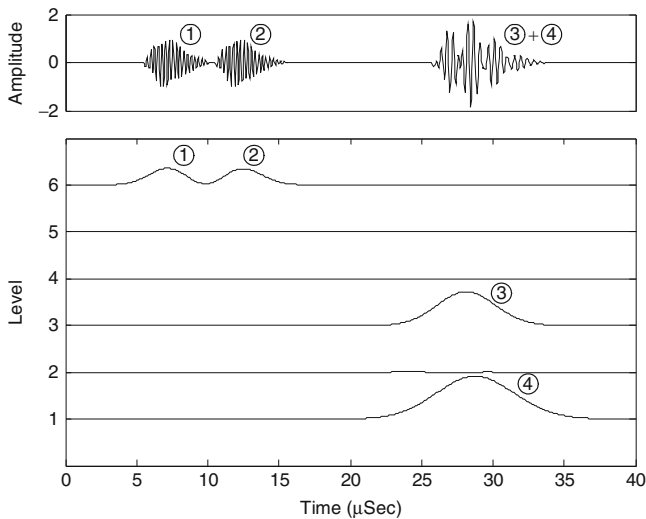


**Fig. 6.6** Detection and differentiation of two pulse trains that are timely overlapped and spectrally adjacent and two pulse trains that are timely adjacent but spectrally identical

temporally (successive along the time axis, with 5  $\mu$ s separation). Similarly, the two pulses ③ and ④ are well separated into the first and third levels, reflecting on the different center frequencies that they contain.

### 6.3.1.2 Experimental Study

To experimentally verify the performance of the developed multiscale enveloping technique for ultrasonic pulse detection, three ultrasonic transmitters were designed and prototyped, with the center frequencies being 2,480, 2,785, and 3,140 kHz, respectively. An electrical pulser (model C-101-HV from PAC company) was used to electrically excite the transmitters. Ultrasonic pulses generated were then transmitted through a steel block of 6 cm thickness, which represents a realistic injection mold. The pulses were received by an ultrasonic receiver located on the opposite side of the steel block. The received ultrasonic pulses were measured and recorded using a digital oscilloscope (model TDS 3012B from Tektronix).

In the first experiment, a single transmitter (center frequency 3,140 kHz) was excited repetitively at 10 kHz. As a result, a series of pulses were generated with two adjacent pulses being timely separated by 100  $\mu$ s, as shown in Fig. 6.7a. For each train of pulses generated (by each excitation), the first arrived pulse with the highest amplitude, plus two reflections with decaying amplitudes were clearly observed. The received pulses were processed using the multiscale enveloping technique, and their corresponding envelopes were extracted. As shown in Fig. 6.7a, the first arrival and the first two reflections were clearly differentiated at level 4. As the reflections have much lower amplitude than the first arrival, they

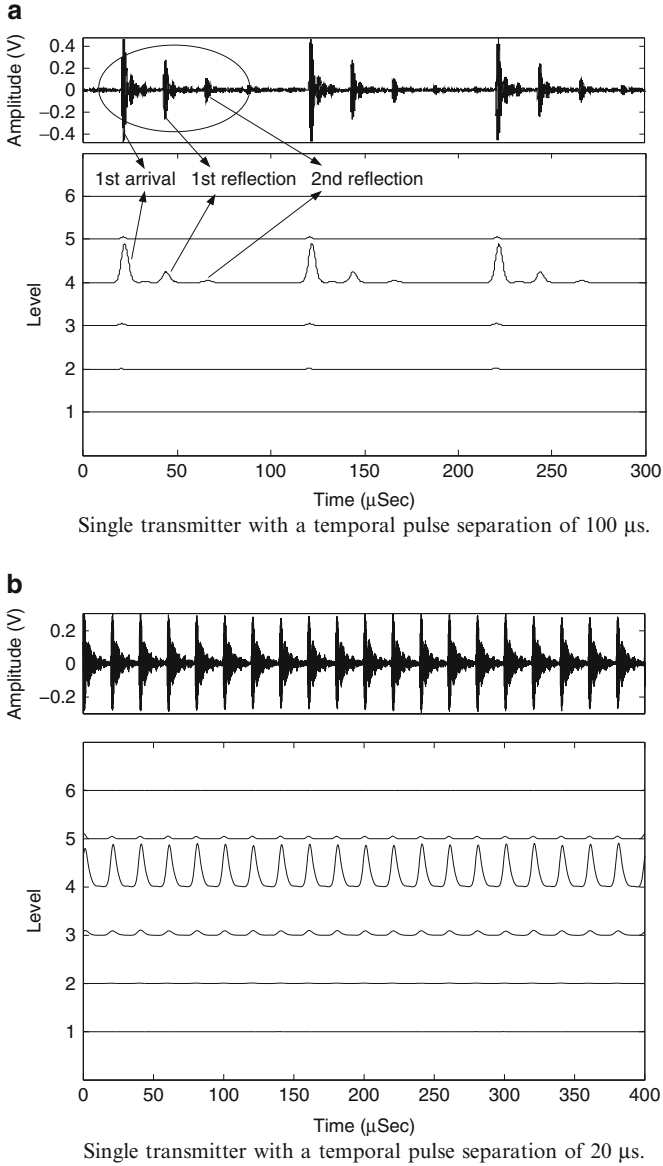


**Fig. 6.7** Experimental detection of ultrasonic pulse trains having the same center frequency. (a) Single transmitter with a temporal pulse separation of 100  $\mu\text{s}$  and (b) single transmitter with a temporal pulse separation of 20  $\mu\text{s}$

can be readily eliminated through thresholding from the extracted envelope. In the second experiment, the pulse repetition frequency was increased to 50 kHz, resulting in a temporal separation of 20  $\mu\text{s}$  between the adjacent pulses. As shown in

Fig. 6.7b, the reflections were buried under the first arrivals; therefore, they did not affect the pulse detection.

To evaluate the pulse detector's ability in differentiating spectrally adjacent pulses in the frequency domain, the three transmitters (of center frequencies 2,480, 2,785, and 3,140 kHz) were placed side-by-side on one side of the steel block and excited simultaneously, with the excitation repetition frequency being 30 kHz (corresponding to 33  $\mu$ s pulse separation). The pulses received by the ultrasonic receiver are shown in the upper portion of Fig. 6.8a, where temporal overlap of the three transmitters cannot be differentiated in the time domain. Applying the multiscale enveloping technique, the envelopes of the three pulse trains were successfully extracted and differentiated in levels 2, 3, and 4, respectively, as shown in Fig. 6.8b.

To examine the robustness of the multiscale enveloping technique, repetition frequency of the excitation input to the transmitters was varied to be 30, 20, and 10 kHz for the three transmitters, resulting in a pulse separation of 33, 50, and 100  $\mu$ s, respectively. As shown in Fig. 6.8b, the pulse trains were again successfully detected and differentiated, with the corresponding envelopes separated into levels 2, 3, and 4, respectively.

### 6.3.2 *Bearing Defect Diagnosis in Rotary Machine*

A large number of applications in machine condition monitoring involve rotary machine components, for example, bearings, spindles, and gearboxes (Kiral and Karagülle 2003; Wu et al. 2004; Choy et al. 2005). To detect structural defects that may occur in these machine components, spectral analysis of the signal's envelope has been widely employed (McFadden and Smith 1984; Ho and Randall 2000). This is based on the consideration that structural impacts induced by a localized defect often excite one or more resonance modes of the structure and generate impulsive vibrations in a repetitive and periodic way. Frequencies related to such resonance modes are often located in higher frequency regions than those caused by machine-borne vibrations, and are characterized by an energy concentration within a relatively narrow band centered at one of the harmonics of the resonance frequency. By utilizing the effect of mechanical amplification provided by structural resonances, defect-induced vibration features can be separated from the background noise and interference for diagnosis purpose. However, as different resonance modes can be excited under varying machine operating conditions, consistent results are not guaranteed by simply applying the traditional enveloping spectral analysis. Research has found that complementing the wavelet-based multiscale enveloping with spectral analysis by means of the multiscale enveloping spectrogram (MuSenS) technique could significantly enhance the effectiveness of bearing defect diagnosis (Yan and Gao 2005b). Basically, the MuSenS starts with a signal's envelope extraction by using the developed wavelet-based multiscale enveloping technique; Fourier transform is then performed repetitively on the extracted

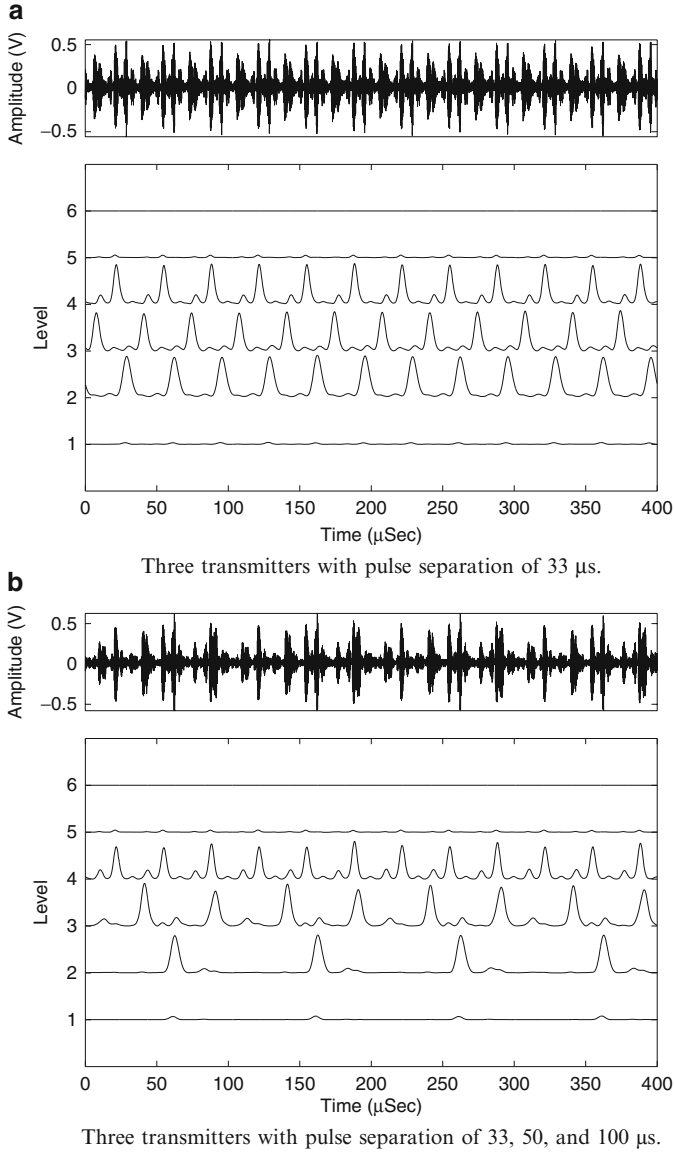


**Fig. 6.8** Experimental detection and differentiation of temporally overlapped and spectrally adjacent ultrasonic pulse trains generated by three transmitters. (a) Three transmitters with pulse separation of 33 μs and (b) three transmitters with pulse separation of 33, 50, and 100 μs

envelope signal  $env_{wt}(s, \tau)$  at each scale  $s$ , resulting in an “envelop spectrum” of the original signal at the various scales. Such envelop spectra can be expressed as

$$ENV_{wt}(s, f) = F[env_{wt}(s, \tau)] = \frac{1}{2\pi} \int_{-\infty}^{\infty} \|wt_c(s, \tau)\| e^{-i2\pi f\tau} d\tau \quad (6.16)$$

where the envelope signal  $env_{wt}(s, \tau)$  is obtained using (6.15), and calculated directly from the modulus of the wavelet coefficients  $\|wt_c(s, \tau)\|$  of the original signal. The result of the  $ENV_{wt}(s, f)$  operation is a 2D matrix, with each of its rows corresponding to the envelop spectrum of the vibration signal at a specified scale  $s$ , and each of its columns corresponding to a specific frequency component of the envelope spectrum across all the scales. By looking at the square of the magnitude of  $ENV_{wt}(s, f)$ , as seen in

$$E(s, f) = |ENV_{wt}(s, f)|^2 \quad (6.17)$$

which is termed as the energy spectrum, the final output  $E(s, f)$  of the MuSEnS is obtained. The energy spectrum indicates how the energy content is distributed in the scale-frequency plane. For the purpose of visualization, such a result can be illustrated in a 3D scale-frequency-energy map, which can indicate the intensity and location of the defect-related frequency lines. The applications of the MuSEnS technique to bearing defect diagnosis are introduced in the next section.

### 6.3.2.1 Numerical Simulation Using the MuSEnS Algorithm

A synthetic signal that consists of different signal components for simulating vibration signal from the rolling element bearing is first constructed to quantitatively evaluate the MuSEnS technique. Generally, vibration signals from a bearing may include the following constituent components:

1. vibration caused by bearing imbalance with a characteristic frequency of  $f_u$ , equal to the bearing rotational speed, which occurs when the gravitational center of the bearing does not coincide with its rotational center
2. vibration caused by bearing misalignment at frequency  $f_m$ , equal to twice the shaft speed, which occurs when the two raceways of the bearing (inner and outer) fall out of the same plane, resulting in a raceway axis that is no longer parallel to the axis of the rotating shaft
3. vibration due to rolling elements periodically passing over a fixed reference position on the outer raceway, at the frequency  $f_{BPFO}$
4. structure-borne vibration attributed by other components, which is broadband in nature, and can be modeled as white noise.

When a localized structural defect occurs on the surface of the bearing raceways (inner or outer), a series of impacts will be generated every time the rolling elements interact with the defects, subsequently exciting the bearing system. Such forced vibration is represented by high-frequency resonances that are amplitude modulated at the repetition frequency of the impacts.

For the numerical simulation, only defect-induced resonant vibration and structure-borne vibration are considered in the synthetic signal, as other vibration components can be filtered out through data preprocessing. The simulated resonant

vibration is obtained experimentally from the measured impulse response of a ball bearing (model 2214). This bearing has 17 rolling elements. When it rotates at 300 rpm, a total of eight impacts will be generated per bearing revolution, because of the ball–defect interactions. This translates into an impact interval of 25 ms or a 40-Hz signal repetition frequency. Figure 6.9a illustrates such a series of impact-related vibrations. By adding white noise to these vibrations, a synthetic signal is then generated to simulate the actual bearing vibrations due to a localized outer raceway defect. The signal-to-noise ratio (SNR) of the synthetic system is set at  $-12$  dB. The synthetic signal with its time and frequency domain waveform is shown in Fig. 6.9b, c. Because of the noise corruption, no apparent signal feature could be identified, except for the relatively dominant spectral components ranging from 2,500 to 3,500 Hz.

The synthetic signal is analyzed using the wavelet-based MuSenS technique, where the complex Morlet wavelet is used as the base wavelet for defect characteristic extraction. A series of equally spaced scales ranging from 1 to 6 (with an increment of  $s_1$ ) were chosen to stretch the complex Morlet wavelet for extracting the defect-related feature embedded in the synthetic signal. The lower and upper limits of the scales correspond to the wavelet center frequency at 10,000 and

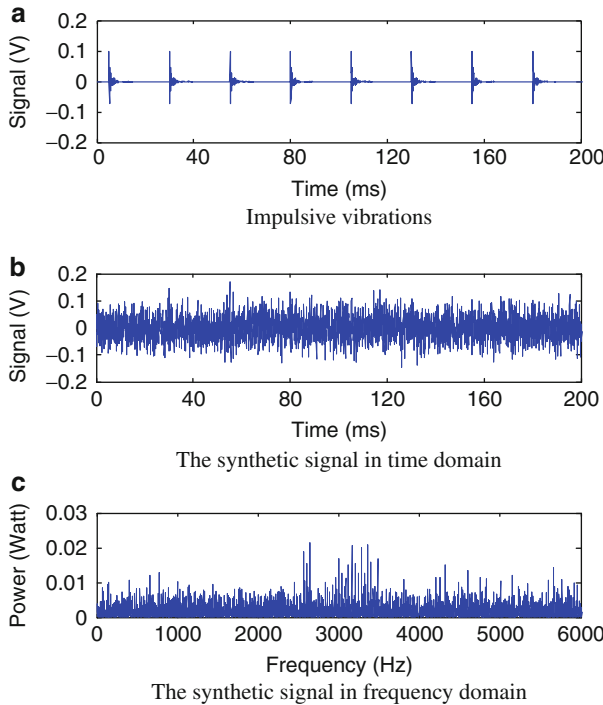


**Fig. 6.9** The series of impulsive vibrations, the synthetic signal (signal-to-noise ratio (SNR) =  $-12$  dB), and its spectrum. (a) Impulsive vibrations, (b) the synthetic signal in time domain, and (c) the synthetic signal in frequency domain

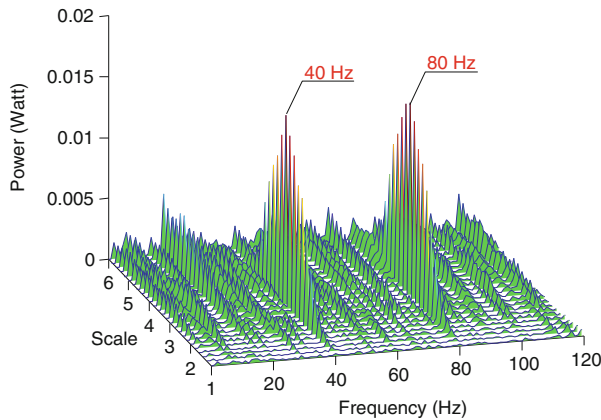


**Fig. 6.10** Defect repetition frequency detection on the synthetic signal using multiscale enveloping spectrogram (MuSEnS) technique

1,667 Hz, respectively. This ensures that the defect-induced resonant vibration component can be fully covered by the wavelet transformation. To increase the possibility of matching the center frequency of a scaled wavelet with the frequency of the defect-induced resonant vibration, a small-scale interval is preferred. However, a small-scale interval leads to increased computational load, as more scales will be involved in the signal decomposition. A trade-off must therefore be made between the accuracy and computational time. On the basis of preliminary studies, an increment of  $s_1 = 0.2$  was employed in this study. As the MuSEnS shown in Fig. 6.10, high-energy concentration can be identified at the 40-Hz frequency line, which corresponds to the defect-related repetition frequency. Also strongly represented in the spectrogram is the harmonics of the defect-related frequency at 80 Hz. This result demonstrates the effectiveness of the *MuSEnS* algorithm in identifying defect features hidden in bearing vibration signals.

### 6.3.2.2 Case Study

The first experimental case study of using *MuSEnS* algorithm to diagnose bearing defects is conducted on a roller bearing. A seeded defect in the form of 0.1 mm diameter hole is made in the outer raceway. The bearing is subject to a 3,665-N radial load, and the shaft rotational speed is 1,200 rpm (or a 20-Hz rotational frequency). On the basis of the geometrical parameters of the bearing and the rotational speed, a defect-related repetitive frequency of ( $f_{\text{BPFO}} = 5.25f_{\text{rpm}}$ ) or 105 Hz can be analytically determined (Harris 1991). Figure 6.11 shows the bearing vibration signal acquired under the sampling frequency of 25 kHz. From its corresponding power spectrum, it is evident that frequency component related to bearing rotation is dominant in the frequency region of [0, 150] Hz. However,

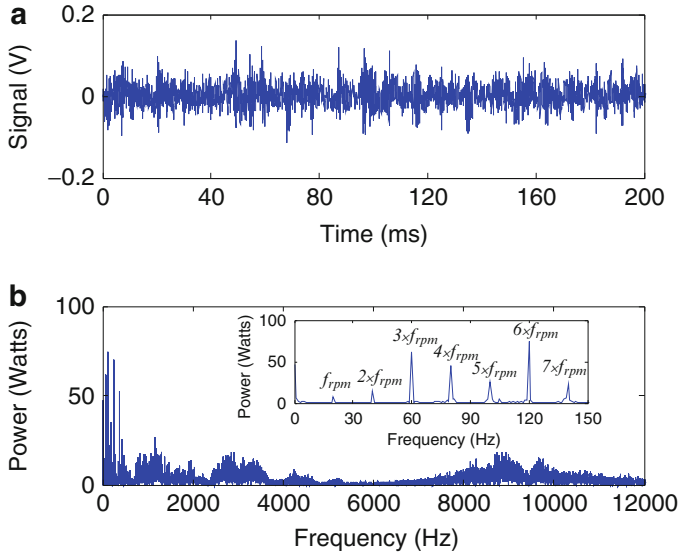


**Fig. 6.11** Signal measured from a roller bearing and its power spectrum

defect-related frequency component of 105 Hz is submerged in the spectrum and therefore, cannot be identified.

The *MuSEnS* algorithm is then applied to decompose the bearing signal. The scales used are between 1 and 8, with an increment 0.2. These scales cover the frequency range of 1.56–12.5 kHz. The corresponding *MuSEnS* of the bearing vibration signal is shown in Fig. 6.12. Two major peaks are clearly shown at 20 and 105 Hz frequency lines, respectively. The 20-Hz component runs across the entire scale region, and is related to the bearing rotating speed. The 105-Hz component is identified at the scales of 1–2.4, and represents the repetitive frequency of the bearing due to the structural defect on the outer raceway. This demonstrates that the *MuSEnS* is able to clearly identify the existence of the structural defect, and pinpoint its location on the outer raceway for diagnosis purpose.

The second experimental case study of using the *MuSEnS* algorithm for diagnosis of bearing inner raceway defect is investigated on a ball bearing of model SKF 6220. The defect-related repetitive frequency is calculated to be ( $f_{BPEI} = 5.9f_{rpm}$ ) or 59 Hz, based on the bearing geometry and rotational speed (600 rpm) (Harris 1991). A radial load of 10,000 N is applied to the bearing. As shown in Fig. 6.13, while frequency components related to the shaft speed and ball rotation are shown in the power spectrum, the defect-related repetitive frequency is not identified.

The *MuSEnS* algorithm is then applied to the same signal, with the decomposition scales chosen to be  $\sim 2$ –10 at an increment of 0.2. The scales cover the frequency range from 500 to 2,500 Hz. As shown in Fig. 6.14, besides frequency components related to the shaft frequency and its harmonics, an appreciable peak can be seen at 59 Hz, which is the inner raceway defect-related repetitive frequency. This indicates that a structural defect exists on the inner raceway of the ball bearing. The peaks at 49 and 69 Hz frequency lines are attributed to the combined effect of



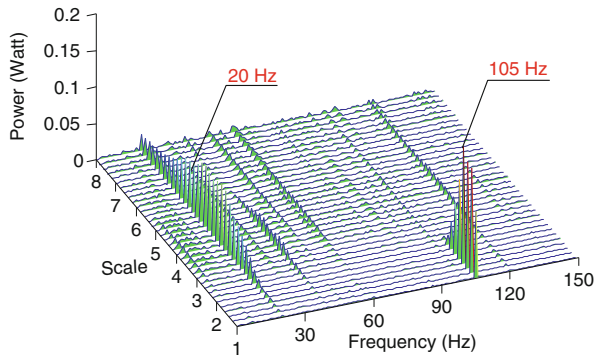


**Fig. 6.12** MuSenS of vibration signals measured on a roller bearing with a structural defect on the outer raceway (speed: 1,200 rpm; radial load: 3,665 N)

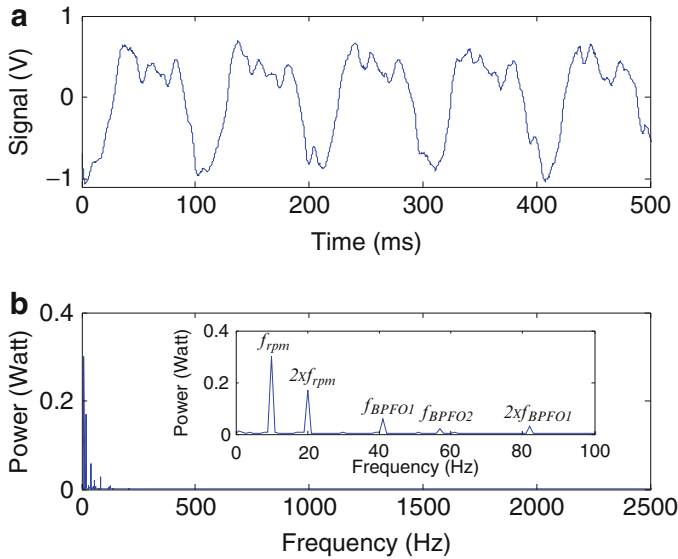


**Fig. 6.13** Signal measured from a ball bearing and its power spectrum

bearing imbalance at 10 Hz frequency and the structural defect at 59 Hz frequency, as they can be calculated as  $59 \pm 10$  Hz.

## 6.4 Summary

A wavelet-based multiscale enveloping technique is introduced in this chapter. This multidomain signal processing technique combines band-pass filtering (implemented through variation of the scale parameter  $s$  of the base wavelet) and enveloping

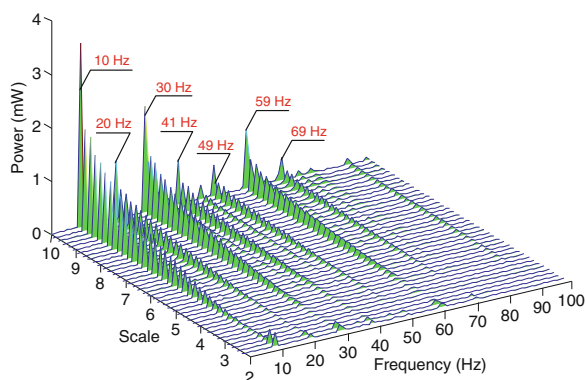


**Fig. 6.14** MuSenS of vibration signals measured on a ball bearing with a structural defect on the inner raceway (speed: 600 rpm; radial load: 10,000 N)

(obtained through modulus of the wavelet coefficients) into a *single-step* operation. The effectiveness of the multiscale enveloping technique is demonstrated through studies in ultrasonic pulse differentiation for pressure measurement in injection molding and bearing defect diagnosis in rotary machines, both numerically and experimentally.

When the multiscale enveloping technique is used to identify the ultrasonic pulses generated from injection molding process, not only spectrally identical and timely adjacent but also timely overlapped and spectrally adjacent ultrasonic pulses could be detected and differentiated. This allows for comprehensive spatial coverage of the cavity pressure profile by placing multiple sensors with different working frequency ranges at different locations in the injection mold. When the wavelet-based enveloping is combined with spectral domain postprocessing, a new algorithm termed MuSenS was developed, which has been shown to be more accurate and illustrative in depicting critical features related to structural defects embedded in the bearings than the traditional enveloping spectral analysis. As many of the applications in manufacturing equipment and system monitoring involve rotary machine components (e.g., bearings, spindles, gearboxes, etc.), it is possible that the MuSenS technique may contribute to improving solutions to a wide variety of machine monitoring problems.

## 6.5 References

- Choy FK, Zhou J, Braun MJ, Wang L (2005) Vibration monitoring and damage quantification of faulty ball bearings. *ASME J Tribol* 127(3):776–783

- Gao R, Kazmer D, Theurer C, Zhang L (2001) Fundamental aspects for the design of a self-energized sensor for injection molding process monitoring. In: Proceedings of NSF design and manufacturing research conference, Tempa, FL
- Greguss P (1980) Ultrasonic imaging: seeing by sound. The principles and widespread applications of image formation by sonic, ultrasonic, and other mechanical waves. Focal Press, New York
- Hahn SL (1996) Hilbert transform in signal processing. Artech House Inc., Norwood, MA
- Harris TA (1991) Rolling bearing analysis, 3rd edn. Wiley, New York
- Ho D, Randall RB (2000) Optimization of bearing diagnostic techniques using simulated and actual bearing fault signals. *Mech Syst Signal Process*, 14(5):763–788
- Kiral Z, Karagülle H (2003) Simulation and analysis of vibration signals generated by rolling element bearing with defects. *Tribol Int* 36:667–678
- Lawrence MS (1999) Computing the discrete time analytic signal via FFT. *IEEE Trans Signal Process* 47(9):2600–2603
- Lee BY, Tang YS (1999) Application of the discrete wavelet transform to the monitoring of tool failure in end milling using the spindle motor current. *Int J Adv Manuf Technol* 15(4):238–243
- Liang W, Que PW, Yang G (2006) Ultrasonic flaw detection during NDE of oil pipelines via a resonance filter. *Russ J Nondestruct Test* 42(6):398–403
- McFadden P, Smith J (1984) Vibration monitoring of rolling element bearings by the high frequency resonance technique – a review. *Tribol Int* 17(1):3–10
- McGonnagle WJ (1966) Nondestructive testing, 2nd edn. Gordon and Breach Science Publisher, New York
- Oppenheim AV, Schafer RW, Buck JR (1999) Discrete-time signal processing, 2nd edn. Prentice Hall, Upper Saddle River, NJ
- Prabhakar S, Mohanty AR, Sekhar, AS (2002) Application of discrete wavelet transform for detection of ball bearing race faults. *Tribol Int* 35:793–800
- Rawabdeh IA, Petersen PF (1999) In-line monitoring of injection molding operations: a literature review. *Injection Molding Technol* 3:47–53
- Theurer C, Zhang L, Gao R, Kazmer D (2001) Acoustic telemetry in injection molding. In: Proceedings of society of plastics engineers annual technical conference, process monitoring and control division, vol 51. Dallas, TX, pp 208–213
- Tse PT, Peng YH, Yam R (2001) Wavelet analysis and envelope detection for rolling element bearing fault diagnosis – their effectiveness and flexibilities. *ASME J Vib Acoust* 123(4):303–310
- Wang W (2001) Early detection of gear tooth cracking using the resonance demodulation technique. *Mech Syst Signal Process* 15(5):887–903
- Wu JD, Huang CW, Huang R (2004) An application of a recursive Kalman filtering algorithm in rotating machinery fault diagnosis. *NDT&E Int* 37:411–419
- Yan R, Gao R (2005a) An efficient approach to machine health evaluation based on harmonic wavelet packet transform. *Robot Comput Integrated Manuf* 21:291–301
- Yan R, Gao R (2005b) Multi-scale enveloping spectrogram for bearing defect detection. *World tribology congress III*, Washington, DC, pp 855–856
- Yen G, Lin K (2000) Wavelet packet feature extraction for vibration monitoring. *IEEE Trans Ind Electron* 47(3):650–667
- Yoshida A, Ohue Y, Ishikawa H (2000) Diagnosis of tooth surface failure by wavelet transform of dynamic characteristics. *Tribol Int* 33:273–279
- Zhang L, Theurer C, Gao R, Kazmer D (2004) A self-energized sensor for wireless injection mold cavity pressure measurement: design and evaluation. *ASME J Dyn Syst Meas Control* 126(2):309–318